

Dynamical Effects of Colliding Outflows in Binary Systems

LILE WANG^{1,2} AND XINYU LI^{3,4}

¹*The Kavli Institute of Astronomy and Astrophysics, Peking University, Beijing 100084, China; lilew@pku.edu.cn*

²*Center for Computational Astrophysics, Flatiron Institute, 162 5th Ave, New York, NY 10010, USA*

³*Canadian Institute for Theoretical Astrophysics, 60 St George St, Toronto, ON, M5R 2M8, Canada*

⁴*Perimeter Institute for Theoretical Physics, 31 Caroline Street North, Waterloo, ON, N2L 2Y5, Canada*

ABSTRACT

The outflow of an object traveling in a fluid can shape the fluid morphology by forming a forward bow shock which accelerates the object via gravitational feedback. This dynamical effect, namely “dynamical anti-friction”, has been studied in idealized infinite uniform media, which suffers from the convergence problem due to the long-range nature of gravitation. In this work, we conduct global 3D hydrodynamic simulations to study this effect in the scenario of a binary system, where the collision of outflows from both stars creates a suitable configuration. We demonstrate with simulations that a dense and slow outflow can give rise to a positive torque on the binary and lead to the expansion of the orbit. As an application, we show that binaries consisting of an AGB star and an outflowing pulsar can experience $\sim 10\%$ orbit expansion during the AGB stage, in addition to the contribution from mass-loss. We also prove that the gravitational force drops as $O(r^{-3})$ from the center of mass in the binary scenarios, which guarantees a quick converge of the overall effect.

Keywords: stars: mass-loss — stars: neutron — stars: winds, outflows — method: numerical

1. INTRODUCTION

Winds and outflows are launched from stellar objects through various mechanisms. For high-mass stars, winds are usually radiatively driven through line absorption (Lamers & Cassinelli 1999) with speed up to $\gtrsim 10^3$ km/s and mass loss rate larger than $10^{-5} M_{\odot}/\text{yr}$. For low-mass stars, the mechanism of driving wind are likely analogous to the solar wind, which is accelerated by the thermal pressure gradient (Parker 1958) with a much lower mass-loss rate ($10^{-14} M_{\odot}/\text{yr}$ for the solar wind). As a low or intermediate-mass star evolves into the asymptotic giant branch (AGB) phase, slow (~ 10 km/s) and dense ($\dot{M} \sim 10^{-8} - 10^{-4} M_{\odot}/\text{yr}$) are launched from the star as the fast wind originating from the stellar remnants interacts with the inner layer of the expanding stellar envelope (Habing & Olofsson 2004; Ramstedt et al. 2008). Besides, strong outflows can be launched from the compact objects either by the strong magnetic fields in the form of pulsar winds or by super-Eddington accretion in the case of SS433 (Fabrika 2004).

In an isolated binary system where a secondary star is orbiting around the primary star, the secondary star exerts a gravitational drag on the wind materials from the primary and accretes a fraction of it. This accretion process of wind materials can occur in high-mass

X-ray binaries (see Shakura et al. 2015 for a review on wind accretion) and is described by the standard Bondi-Hoyle-Lyttleton (BHL) accretion (Hoyle & Lyttleton 1939; Bondi & Hoyle 1944; Edgar 2004). Incoming materials with impact parameters inside a cylinder of the Bondi radius

$$R_B = \frac{2GM}{c_s^2 + V_*^2} \quad (1)$$

are accreted onto the star, while materials with greater impact parameters accumulate behind the star, forming an over-dense wake which acts gravitationally to decelerate the star, known as the dynamical friction (Chandrasekhar 1943; Ostriker 1999). Here, G is the Newtonian gravitational constant, M and V_* are the mass and velocity of the star, respectively, and c_s is the sound speed of the ambient materials. As the secondary star moves around the host star, the over-dense wake is trailing behind the orbit and is expected to dampen the orbital motion and shrink the orbital separation of the two stars. Previous analytical and numerical study (Stahler 2010; Antoni et al. 2019) of binary accretion over a dense gaseous medium confirmed the orbital decay due to dynamical friction.

The picture of dynamical friction needs to be reconsidered when the secondary star also has outflows. The

collision of the strong outflow from the secondary with the incoming materials forms a bow shock around of the secondary (Wilkin 1996; Gaensler 2005). Incoming materials will stream along the shock front away from the secondary, and the accretion is shut off, leaving a low-density bubble behind the secondary. Gruzinov et al. (2020) calculated the gravitational force from the bow shock and found that the net force can accelerate the star given the outflow is strong enough. This phenomenon is proved by numerical simulations (Li et al. 2020) for a star moving in an idealized uniform gas. Similar effects in the planetary discs where thermal luminosities injected from the hot planet lead to a net force opposite to the dynamical friction (Masset & Velasco Romero 2017; Masset 2017; Eklund & Masset 2017; Hankla et al. 2020).

However, previous numerical studies on dynamical friction or anti-friction are usually set up as a local “wind-tunnel” simulation (e.g. MacLeod et al. 2017; Li et al. 2020; De et al. 2020) with an idealized infinite background gas of uniform density or with density gradient. This setup suffers from the convergence problem caused by the long-range nature of gravitation. No matter how far away, matters behind the star will be gravitationally dragged by the star and decelerate the star. The deceleration increases logarithmically with the size of the computational box. Therefore results with uniform gas cannot draw realistic conclusions on the orbital evolution of the binary. Global simulations with realistic gas distribution are required and have been applied to study dynamical friction (Schröder et al. 2021).

This paper performs 3D global realistic simulations of a binary system with outflows launched from both stars. We focus on how the interactions between the outflows shape the orbital evolution of the binary systems. Unless specified, we present our results with all physical quantities in the code unit with mass m_c , length ℓ_c , and time t_c .

This paper is structured as follows. In §2 we briefly introduce the numerical methods, the general setups of problems, and some key diagnostic quantities for post-simulation analyses. §3 discusses an idealized binary that consists of two nearly identical stars and explores the impact from different physical parameters using a few series of extra models. We apply our calculation to a specific model of an AGB-pulsar binary in §4. Discussion and conclusion are presented in §5 where we prove that we obtain robust results which are convergent and independent of the computational box size.

2. METHODS

2.1. Basic Geometry and Configurations

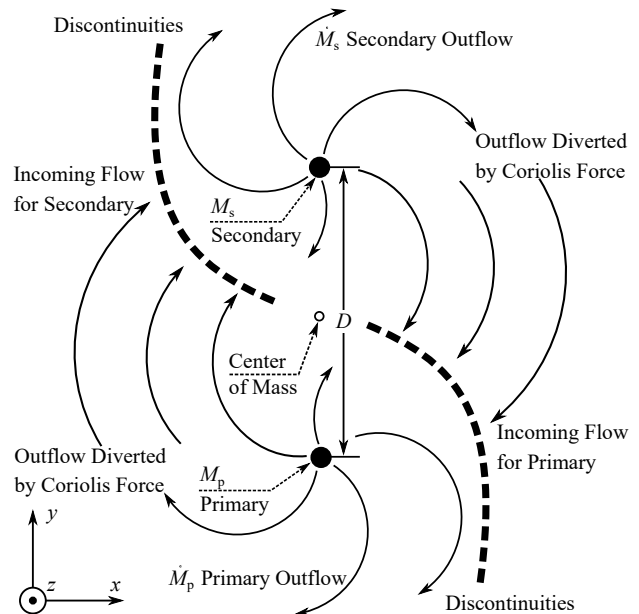


Figure 1. Simulation setups in the co-rotating frame. The two stars with mass $M_{p,s}$ are fixed on the y -axis and separated by distance D . Outflows are launched from the two stars with mass-loss rates $\dot{M}_{p,s}$. Details of the outflow colliding regions are omitted in this figure. We simply annotate “Discontinuities” generically for the relevant phenomena.

We simulate the evolution of a binary system consisting of a primary star and a secondary star on a Cartesian grid in their *co-rotating frame*. The setup is illustrated by Figure 1. The subscripts “p” and “s” denote the quantities associated with the primary and the secondary star throughout this paper, respectively.

The two stars are located along the y -axis, separated by distance D and orbit each other on a circular orbit. For convenience, we denote the star on the negative half of the y -axis as the primary, and the one on the positive half as the secondary with mass $M_{p,s}$ respectively. The y -coordinates of the stars are set as $y_p = -DM_s/(M_s + M_p)$ and $y_s = DM_p/(M_s + M_p)$, so that the center of mass is fixed at the origin.

Rectangular boxes define the simulation domains in this paper, in which Cartesian grids are used. The orbital angular velocity vector is parallel to the z -axis, so that the orbit stays in the $z = 0$ plane. Due to the system geometry, we assume reflection geometry over the $z = 0$ plane and adopt a reflecting boundary condition at that plane; outflowing boundary conditions are adopted elsewhere. The simulation domain size is defined by box size L_{box} : the domain spans a sub-space $\{x, y, z\}/(L_{\text{box}}/2) \in [-1, 1] \otimes [-1, 1] \otimes [0, 1]$. We denote the resolution of the unrefined base grid with N_0 as $N_x \times N_y \times N_z = N_0 \times N_0 \times (N_0/2)$, which yields unitary aspect ratios. We set up multiple levels of static

mesh refinement near the source regions to resolve each source radius by at least three cells. All simulations are run till steady or quasi-steady states are reached.

2.2. Numerical Hydrodynamics

We use a newly developed, GPU-optimized code *Kratos* (L. Wang, in prep.) to numerically evolve the hydrodynamic equations for the dynamics of the outflowing gas,

$$\begin{aligned} \frac{\partial \rho}{\partial t} + \nabla \cdot (\rho \mathbf{v}) &= 0, \\ \frac{\partial(\rho \mathbf{v})}{\partial t} + \nabla \cdot (\rho \mathbf{v} \mathbf{v} + p \mathbf{I}) &= -\rho \nabla \Phi, \\ \frac{\partial \epsilon}{\partial t} + \nabla \cdot [\mathbf{v}(\epsilon + p)] &= -\rho \mathbf{v} \cdot \nabla \Phi. \end{aligned} \quad (2)$$

Here, ρ , \mathbf{v} , p and ϵ are the mass density, velocity, gas pressure, and total energy density, respectively, Φ is the gravitational potential, and \mathbf{I} is the identity tensor. In the *Kratos* framework, hydrodynamic solvers are employed by the higher-order Godunov method, involving piecewise-linear method (PLM) reconstruction with minmod slope limiter, HLLC Riemann solver, and second-order Runge-Kutta time integrator for second-order accuracy in both space and time (see e.g. [Toro 2011](#)).

Eqs. (2) are integrated in the co-rotating frame with the binary angular frequency $\Omega = [G(M_p + M_s)/D^3]^{1/2}$. The centrifugal acceleration \mathbf{a}_{cf} and Coriolis acceleration \mathbf{a}_{co} in this rotating frame read,

$$\mathbf{a}_{\text{cf}} = \boldsymbol{\Omega} \times (\mathbf{x} \times \boldsymbol{\Omega}), \quad \mathbf{a}_{\text{co}} = -2\boldsymbol{\Omega} \times \mathbf{v}, \quad (3)$$

which are fed as the additional source terms into eq. (2). Here $\boldsymbol{\Omega}$ is the angular velocity vector, and we denote P to be the orbital period. Note that these two terms are specific to Cartesian meshes; their effects can be included in the simulations in spherical-polar and cylindrical coordinates naturally without actually referring to the source terms (see also [Kley 1998](#)).

The two stars source the gravitational potential for eq. (2) and we neglect the self-gravity of the gas. Both stars also serve as “source particles” (see e.g. [Murray et al. 2017](#)) to launch isotopic outflows. In the adjacency of each star, we set up a spherical “source region” with radius r_{src} , in which an initial radial velocity v_{src} is set as a model parameter. The density is set to produce the desired mass-loss rate $\dot{M} = 4\pi r^2 \rho v_{\text{src}}$. The gas pressure is set based on a chosen temperature parameter p/ρ . The physical quantities are fixed during the hydrodynamic evolution, producing constant outflows from the source regions.

We adopt the ideal equation of state for the gas with a fixed ratio of heat capacity γ . It is well-known that

an adiabatic hydrodynamic system with a central point source of gravity cannot sustain steady supersonic outflows if $\gamma \geq 3/2$ (e.g. [Parker 1958](#)). Despite the actual states of materials, such outflows could remain $\gamma < 3/2$ due to various heating mechanisms in reality. For simplicity, we adopt a specific γ for each problem within this paper.

2.3. Analyses Schemes

After reaching supersonic regimes, perturbations of fluids can only feedback their impact onto the objects by gravity. We calculate the gravitational acceleration of each star from the gas component by summing over every piece of fluid mass

$$\mathbf{g}_{\text{p},s} = G \int_V dV \frac{\rho \mathbf{x}_{\text{p},s}}{|\mathbf{x}_{\text{p},s}|^3}, \quad (4)$$

where $\mathbf{x}_{\text{p},s}$ are the direction vectors pointing from the primary or the secondary to the gas element, and the integral runs over the whole simulation domain. Since our simulation box only contains the upper half-space, we make use of the reflection symmetry and add the contribution of \mathbf{g} from the lower half-space.

With the fundamental configurations in [Figure 1](#), the secular orbital evolution is only affected by the tangential component of the gravity, g_τ . Constant perturbations on the radial force does not affect any orbital parameters, and the reflection symmetry of the system guarantees zero net force parallel to the axis of angular velocity. Summing up the torques on the two stars, we obtain the relative rate Γ at which the orbital scale D varies,

$$\Gamma \equiv \frac{\dot{D}}{D} = \frac{2(T_p + T_s)}{L_p + L_s} = \frac{2D}{\Lambda} (g_{\tau;p} + g_{\tau;s}). \quad (5)$$

Here, $T_{\text{p},s} = \mu g_{\tau;\text{p},s} D$ are the torques on the primary or secondary, $L_{\text{p},s}$ are the angular momenta with respect to the center of mass, $\mu \equiv M_p M_s / (M_p + M_s)$ is the reduced mass, and $\Lambda = [GD(M_p + M_s)]^{1/2}$ is the reduced specific angular momentum which satisfies $L_p + L_s = \mu \Lambda$. Eqs. (4) and (5) evaluate the key effect concerned in this paper.

To quantify the contribution to the orbit expansion from gas element at different locations, we define τ to be the “torque density” as,

$$\tau = GD\rho\mu \left(\frac{\delta x_p}{r_p^3} - \frac{\delta x_s}{r_s^3} \right), \quad (6)$$

where $\delta x_{\text{p},s}$ and $r_{\text{p},s}$ are the x -direction signed displacement and the distance, measured from the primary and the secondary, respectively. The sign is chosen in such a way that a positive τ leads to positive contribution to Γ . It is also straightforward to verify that $\int_V \tau dV = T_p + T_s$.

3. NEAR-IDENTICAL BINARIES

This section discusses a type of model binaries whose both stars have similar conditions.

3.1. Fiducial Model Setup: Identical Stars

We start with a fiducial model (also Model EM) that contains two identical stars with the same outflow conditions. These two stars with $M_p = M_s = m_c$ are separated by $D = \ell_c$, and orbit each other on a circular orbit with period $P = 2\pi[G(M_p + M_s)/D^3]^{-1/2} = 0.707$ yr. The outflows of both star are characterized by the mass-loss rate $\dot{M}_0 \equiv 4\pi \times 10^{-13} m_c/t_c$, initial pressure-to-density ratio $p/\rho = 10^2 (\ell_c/t_c)^2$, and the initial velocity $v_{\text{src}} = v_0 \equiv 11 \ell_c/t_c$ within the source region $r_{\text{src}} = 0.1 \ell_c$. We set $\gamma = 1.01$ to emulate a near-isothermal condition for the outflowing gas. According to the Parker isothermal wind solution, the outflow should reach $v \sim 33 \ell_c/t_c$ when it reaches the approximates of the companion. We use the box size $L_{\text{box}} = 32 \ell_c$ and the base resolution of 256 zones per L_{box} . Two levels of static mesh refinement are set near the centers of both stars, so that the source region radius r_{src} is resolved by no less than 3 zones.

A convergence test (marked as Model EM-C) is conducted, in which the base resolution is 512 cells per L_{box} , and the number of levels for mesh refinement is kept as 2, to double the resolution everywhere. We also perform another test run (denoted by Model EM-SO) in which the outflow of the secondary is turned off totally. These simulations are run for $t \gtrsim 5.5 P$ to guarantee the convergence to the (quasi-)steady states. The fiducial run takes ~ 12 minutes of wallclock time on a workstation with two NVIDIA RTX 3090 GPUs.

3.2. Fiducial Model Results

We present in Figure 2 the key hydrodynamic profiles on the orbital plane at $t = 5.5 P$ for the fiducial model. The collision of identical outflows creates spiral patterns due to orbital motion. As a result, the qualitative features of fluid configuration required by the dynamical anti-friction effect—a relatively over-dense region between the bow shock and terminal shock, an under-dense region behind the star—indeed yields a torque that increases the angular momentum. We note that the contact discontinuity vanishes by decaying into a continuous contact surface. The two outflows are identical, and no discontinuities appear at the normal collision surfaces. Such continuity remains on both sides when streamlines develop near the contact surface, as the streamlines from both stars have tangential contact when they meet.

The fiducial model orbit expansion rate is shown in the upper panel of Figure 3, in which we find the rate

of orbit increase is $\Gamma \simeq 1.51 \times 10^{-13} t_c^{-1}$. As we can observe from the bottom-right panel, the positive torque (indicated by the “lobes” enclosed by white lines) overcomes the “drawbacks” (enclosed by black lines) mainly by the materials near the discontinuity. Model EM-C is only different by $\sim 2\%$, indicating a good convergence in terms of spatial resolution. Model EM-SO, on the other hand, produces $\Gamma \simeq -1.1 \times 10^{-14} t_c^{-1} < 0$. This result confirms that the outflows from the secondary are essential for dynamical anti-friction. The secondary star will migrate inward under the normal dynamical friction mechanism without the secondary outflow.

The lower panel of Figure 2 examines the spatial convergence of orbit expansion rate by showing the residual of $\Delta\Gamma \equiv |\Gamma - \tilde{\Gamma}(r_{\text{cut}})|$ for different “cutoff” radius r_{cut} . Here $\tilde{\Gamma}(r_{\text{cut}})$ is evaluated by eq. (5), but with the integration zones limited to regions within the distance $r < r_{\text{cut}}$ from the center of mass. The $|\Delta\Gamma|$ profile is enveloped by the $\sim r_{\text{cut}}^{-3}$ power-law, shown in the dotted line. This scaling clearly shows that our simulations will produce a finite, converging orbit expansion rate as we increase the computational box size; the result does not suffer from the divergence caused by idealized uniform background ambient. We will revisit this in §5.2 to prove the scaling law and verify the actual convergence of our calculations.

The rate of orbit expansion in physical units is relatively slow. If we specify the code units by $t_c = 1$ yr, $\ell_c = 1$ AU, and $m_c = 1 M_\odot$, this rate leads to a $\Gamma \simeq 0.15\%$ expansion during the 10^{10} yr (the main-sequence lifetime of a typical solar-like star). The “cost” that each star pays for this expansion during this period is $\sim 10^{-2} M_\odot$, which would result in another $\Gamma \sim 1\%$ orbit expansion. In short, this fiducial model exhibits a case in which dynamical anti-friction enhances the orbital expansion from mass-loss by $\sim 15\%$.

3.3. Exploring the Parameter Space

We conduct a series of simulations to study how the dynamical anti-friction effects depend on the key hydrodynamic and orbital parameters. Only one parameter is modified for each model, and the values of the modified parameters with the corresponding results are presented in Table 1.

In the ideal scenario that an outflowing star plunge into a uniform gas, the acceleration of dynamical anti-friction for strong outflow asymptotes to (see Gruzinov et al. 2020)

$$a_{\text{AF}} \sim 8.18 G\rho_0 R_0. \quad (7)$$

Here ρ_0 is the ambient gas density, and R_0 is the distance of the contact discontinuity ahead of the star, where the momentum flux from the outflow balances the incoming

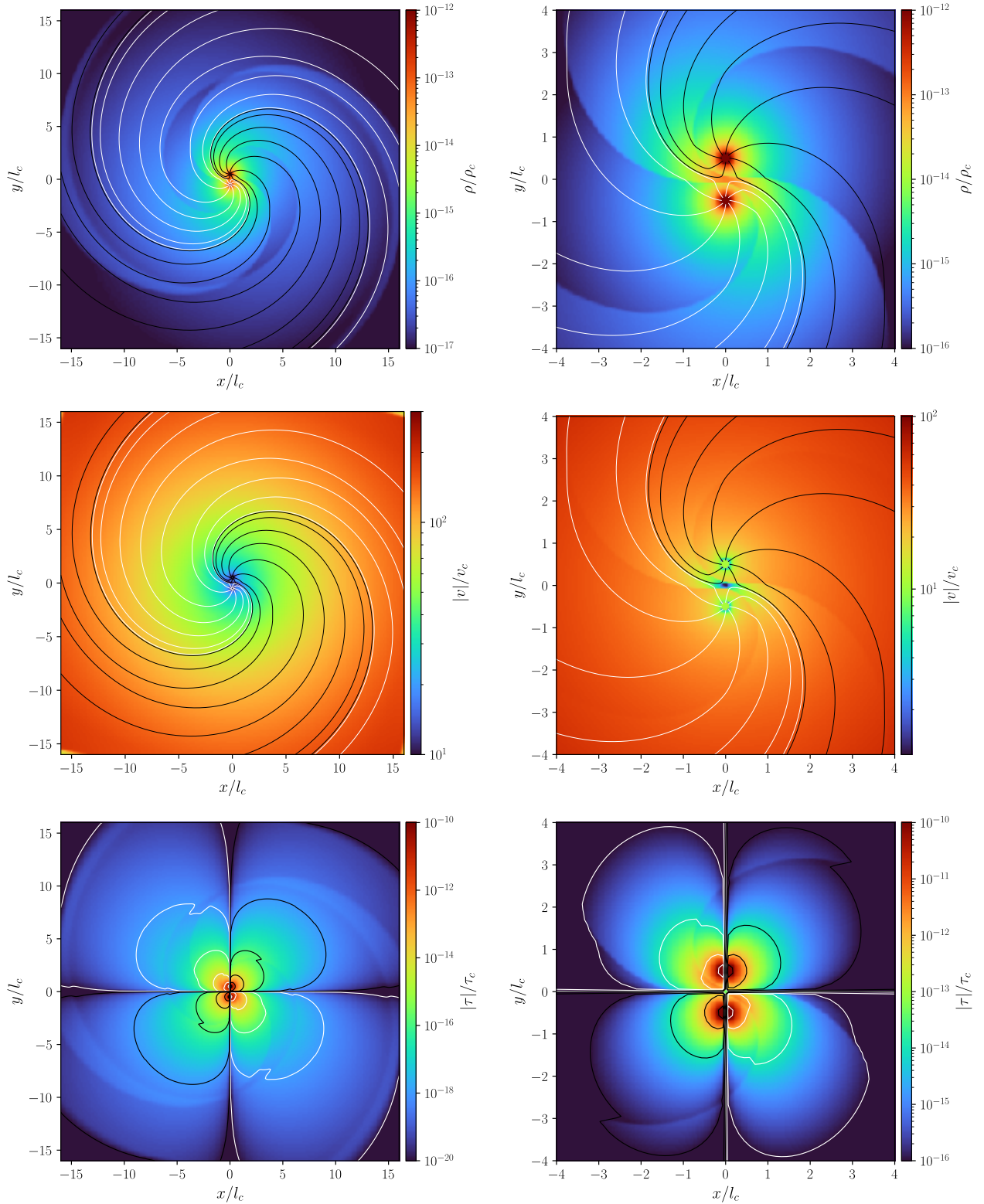


Figure 2. Key hydrodynamic quantities in the orbital plane for the $t = 5.5 P$ snapshot of Model EM (§3.1), including mass density ρ (upper row), the magnitude of co-rotating frame velocity $|v|$ (middle row), and the magnitude of “torque density” $|\tau|$ (lower row; see also §2.3, eq. 6), all normalized by the code units (subscript “c”; $\rho_c \equiv m_c \ell_c^{-3}$, $v_c \equiv \ell_c t_c^{-1}$, and $\tau_c \equiv m_c \ell_c^{-1} t_c^{-2} = p_c$). The left column shows the full cross-section of the domain ($32 \ell_c \times 32 \ell_c$), and the right column zooms in to the $8 \ell_c \times 8 \ell_c$ near the origin. Note that the zoom-in plots may have *different* dynamical ranges. Streamlines are overlaid in each panel except the bottom; black lines are those initiating from the secondary, and white lines from the primary. The contours in the bottom row indicate the magnitudes (on $\lg |\tau/\tau_c| \in \{-20, -18, -16, -12, -10\}$ for the left one, and $\{-18, -16, -12, -10\}$ on the right) and signs (white for positive; black for negative) of the torque density. The outermost black contours are hardly visible.

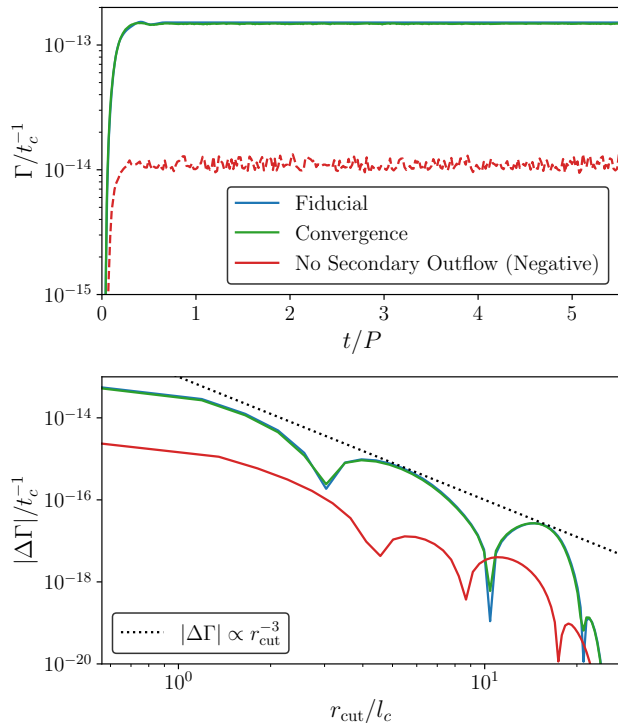


Figure 3. **Upper panel:** relative rate of orbit expansion $\Gamma \equiv \dot{D}/D$ for the fiducial model (Model EM) and its associated tests (distinguished by colors) in §3.2; **negative** numbers are in **dashed lines**. For comparison, the double-resolution convergence test, and the test case with the secondary outflow turned *off* are also presented in different colors. Note that the fiducial model and the convergence test overlap almost perfectly. **Lower panel:** Residual of orbit expansion rate as a function of cutoff radius r_{cut} (measured from the center of mass), compared to the full-domain value (see also §3.2). A dotted line is also plotted to illustrate the $\sim r_{\text{cut}}^{-3}$ scaling.

gas. In the scenario of the binary, we expect the anti-friction to depend on two main factors similar to the case of uniform gas: (1) the ambient gas density ahead of the star where discontinuities are formed, and (2) the balance of the momentum flux between the outflow and the ambient gas, which determines how far away the discontinuities reside.

Models in Series 1 vary the mass-loss rate \dot{M} with invariant v_{src} for both stars. Note that in steady states the scaling $\rho(r) = \dot{M}/4\pi r^2 v(r)$ holds. Essentially, the outflow density changes proportionally as well as the momentum flux $\dot{M}v(r)$. However, the momentum flux ratio for two outflows is kept the same, and the fluid configuration should remain similar. Therefore, the force and torque from the anti-friction are expected to scale linearly with \dot{M} , as confirmed by the results in Table 1.

Table 1. Various models for nearly equal binaries.

Series	Model	Description*	Γ ($10^{-14} t_c^{-1}$)
0	EM	Fiducial	15.1
	EM-C	Convergence Test	14.8
	EM-SO	No Secondary Outflow	-1.1
1	EM-OH	$\dot{M}_{\text{p,s}} = 10 \times \dot{M}_0$	152
	EM-OL	$\dot{M}_{\text{p,s}} = 0.1 \times \dot{M}_0$	1.51
2	EM-VH	$v_{\text{src}} = 3v_0$	10.8
	EM-VL	$v_{\text{src}} = 0.3v_0$	25.6
3	EM-G1	$\gamma = 1.15$	25.5
	EM-G2	$\gamma = 1.4$	67.9
4	EM-DF	$D = 2\ell_c$	5.2
	EM-DN	$D = 0.5\ell_c$	48.9
5	VM-1	$M_s = m_c/2$	14.8
	VM-2	$M_s = m_c/4$	14.0

NOTE—*: Describes the only parameter that it differs from the fiducial model.

Models in Series 2 keep the same \dot{M} and vary v_{src} for the two stars. The outflow density decreases with increasing v_{src} . We find that the orbit expansion rate Γ drops with an increasing v_{src} as expected. There is extra complexity in this case. The increasing outflow velocity makes the acceleration vector more radial rather than tangential, as the tangential component of the “head-wind” should always be Keplerian.

Series 3 varies the adiabatic index γ . The expansion rate is found to increase with γ . Greater γ gives rise to more substantial deceleration of the outflows as they expand outward; therefore, smaller radial velocities but greater densities are met when the outflows reach the interaction region.

In Series 4, we vary the orbital separation D and find that Γ is anti-correlated with D . This is once again the outcome of a greater tangential velocity component as well as a higher gas density at smaller D . The actual scaling shown by Series 4 together with the fiducial model is steeper than linear, because of the complexities brought by the binary motion. By feeding in the physical units, the expansion rate increases super-linearly to $\sim 0.5\%$ per 10^{10} yr for the Model EM-DN with $D = 0.5$ AU, which becomes comparable to the contribution by the mass-loss itself.

Series 5 breaks the assumption of equal mass for the binary and varies M_s , whose results do not exhibit significant difference compared to the fiducial model. The outflows become supersonic when they reach the dynamically important zones, and the gravity from the secondary is not important. Therefore the overall torque is not sensitive to the stellar mass.

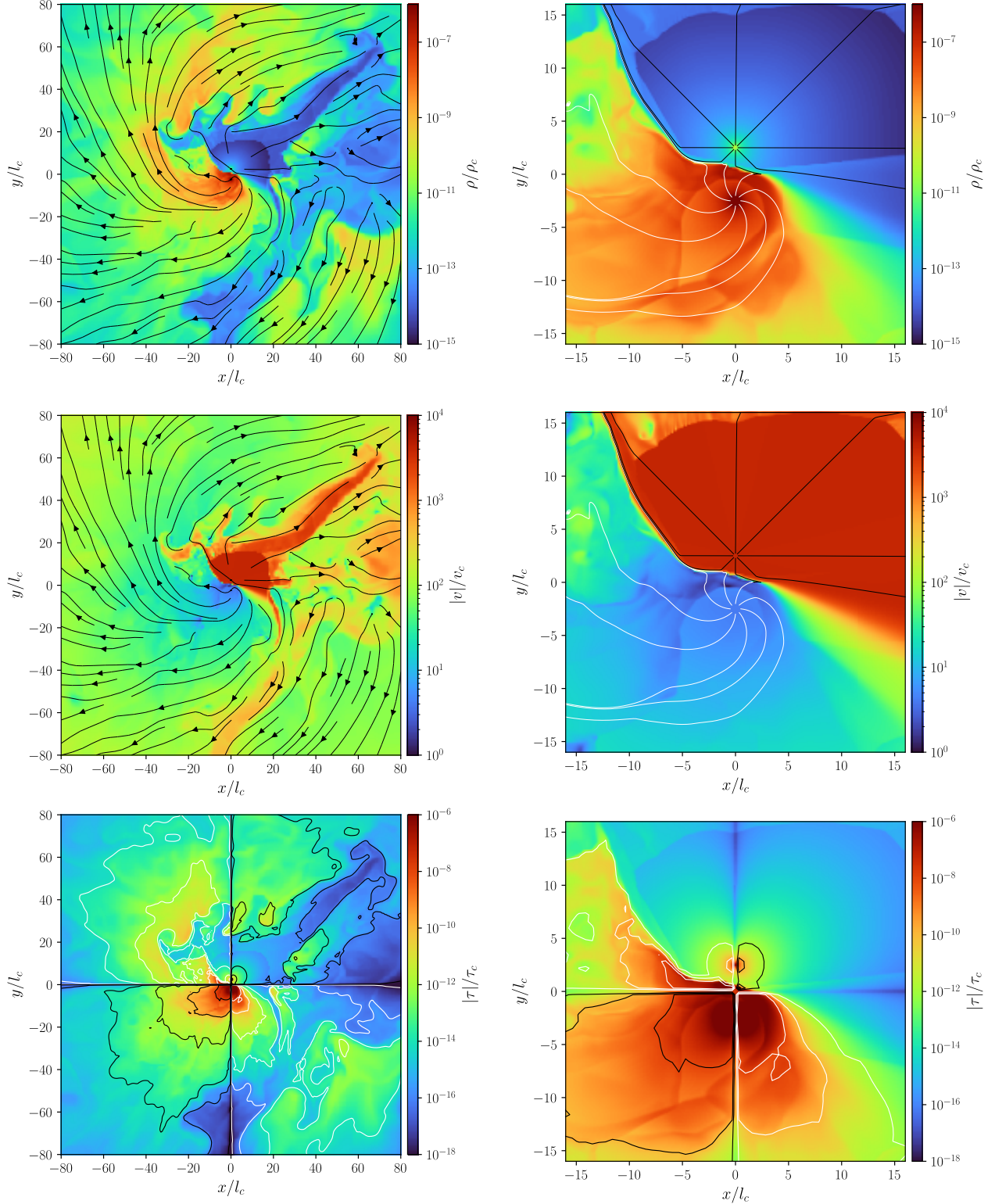


Figure 4. Similar to Figure 2 but for the fiducial AGB-pulsar binary model (Model A0) at the $t = 7 P$ snapshot (orbital period $P \simeq 7.91 t_c$). Note that, because this model exhibits strong shear instabilities, turbulences and mixtures on large scales, we over-plot the streamlines in the left column in a different way. On the bottom row, the contours on the left are laid on $\lg |\tau/\tau_c| \in \{-18, -16, -12, -10, -8\}$, while those on the right indicate $\lg |\tau/\tau_c| \in \{-12, -10, -8\}$.

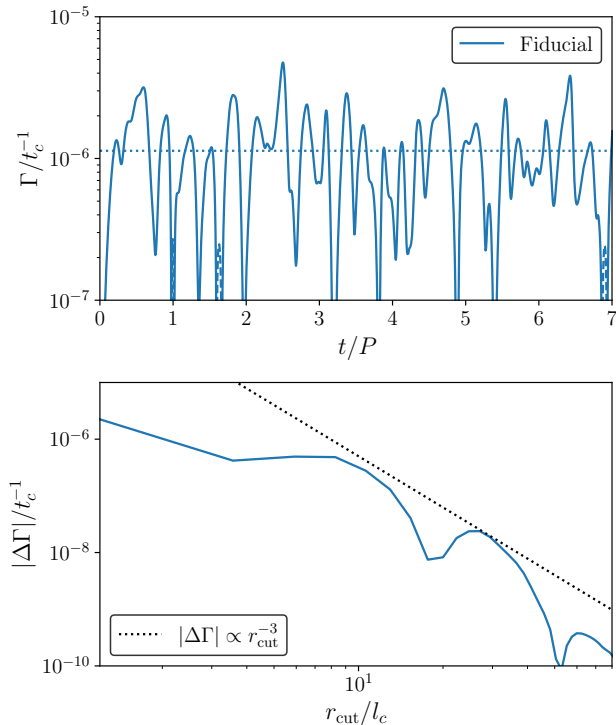


Figure 5. Similar to Figure 3 but for the fiducial model of AGB-pulsar binary (Model A0). A horizontal dotted line is added to the upper panel to illustrate the time-average of the orbit expansion rate.

4. AGB-PULSAR BINARIES

As an application, this section discusses a specific situation of broad interest: an equal-mass binary consists of a wind-blowing pulsar and an AGB star that blows a slower but denser wind. We refer to the AGB as the primary and the pulsar as the secondary for convenience. Previous studies of AGB-related binaries, such as Chen et al. (2018), often consider the cases that the companion is accreting and thus *loses* angular momenta by the interactions with the AGB wind. In this section, we revisit this problem with pulsar companions, whose outflows are usually strong enough to create a hydrodynamic configuration that features an overdense bow-shaped head and an underdense tail, which could be prone to the anti-friction effect.

The AGB outflows deserve extra attention: they are cold ($T \lesssim 10^3$ K) and slow (usually subsonic, a few times ~ 10 km s $^{-1}$), but can still escape from the stellar potential because of radiation pressure on the co-moving dust grains (e.g. Chen et al. 2017, 2020). We adopt a simple recipe that the effective gravitation on the fluids by the primary star is zero, while the full gravity is still used for the orbital motion of the binary itself.

4.1. Fiducial Model Analyses

We use the same code unit conversion as in §3.2 (i.e., $m_c = M_\odot$, $\ell_c = 1$ AU, $t_c = 1$ yr), and setup the fiducial model for AGB-pulsar binary as follows.

Both the primary and the secondary have the same mass as the Sun, $M_p = M_s = M_\odot$, and move at a circular orbit with separation $D = 5$ AU. The primary outflow has mass-loss rate $\dot{M}_p = 1.25 \times 10^{-5} M_\odot \text{ yr}^{-1}$, initial temperature $T_{\text{src,p}} = 1.4 \times 10^3$ K, and initial velocity $v_{\text{src,p}} = 19$ km s $^{-1}$ when it leaves the primary source zone with radius $r_{\text{src,p}} = 0.5$ AU. The secondary is assumed to be a windy pulsar, injecting a pulsar wind with initial temperature $T_{\text{src,s}} = 10^7$ K, velocity $v_{\text{src}} = 1.9 \times 10^4$ km s $^{-1} \simeq 0.064c$, and $\dot{M}_s = 3.8 \times 10^{-8} M_\odot \text{ yr}^{-1}$, from its $R_{\text{src,s}} = 0.25$ AU source zone. As the winds from both stars can easily escape their potential wells, the simulation does not need an isothermal condition to sustain outflows; we use $\gamma = 5/3$ for better capturing the natures of ionized gas hydrodynamics. These parameters correspond to (1) a typical AGB wind that disperses $\sim 50\%$ of its mass during the $\sim 0.5 \times 10^5$ yr AGB period, and (2) an $\dot{E} = 4.3 \times 10^{36}$ erg s $^{-1}$ pulsar wind power, which is on the relatively strong side among the observed windy pulsars (see e.g. Ackermann et al. 2011). Although the spin of pulsars may have excessively high frequency, it should not affect the binary evolution in this work due to separation in scales. Assuming that the pulsar outflow remains rigid co-rotating until the light cylinder, using the conservation of angular momentum for the space beyond, we estimate the effect of spin by the time the pulsar wind reaches the AGB wind,

$$|\Delta v| \sim \frac{Sc^2}{2\pi L} \sim 10 \text{ km s}^{-1} \times \left(\frac{S}{10 \text{ ms}} \right) \left(\frac{L}{0.1 \text{ AU}} \right)^{-1}, \quad (8)$$

where S is the spin period and L is the typical size of outflow collision regions. This $|\Delta v|$ is tiny compared to pulsar winds, allowing us to safely ignore the spin effects.

The computational box has its side length $L_{\text{box}} = 160$ AU, and the co-rotating Cartesian frame is still applied. Three levels of static mesh refinement near the secondary and two levels near the primary are applied to guarantee sufficient resolution: the primary and secondary source zone radii are resolved by no less than three cells. Other simulation setups follow §2.1. We note that simulations of this kind are usually difficult because of significant scale separations in velocities: the speed of binary orbital motion is slower than the pulsar wind by three orders of magnitude. Existing similar simulations are always in 2D and run for a limited num-

ber of periods (e.g. Bosch-Ramon et al. 2012). Eight NVIDIA RTX 3080 GPUs accelerate these simulations, whose total computing speed with the *Kratos* code is roughly equivalent to $\gtrsim 3000$ CPU cores. It takes ~ 3.5 hours wallclock time for a full orbit in our fiducial model, and we run the simulation for seven orbital periods (viz. $t \simeq 7 P$, where $P = 7.91 t_c$).

Figure 4 presents the fundamental hydrodynamic quantities in the orbital plane. Gas near both objects is in distorted “tadpole” shapes. The primary outflow materials dominate the overall torque, while the secondary outflow maintains the spatial configurations by providing substantial ram pressure. The gas velocity exhibits excessive shears near and downstream of the secondary’s terminal shock, leading to significant instabilities in the secondary’s wake. These instabilities result in large fluctuations of the orbital torque shown in the upper panel of Figure 5. The orbital expansion rate shows a time-averaged positive value but fluctuates with a standard deviation comparable to the mean. The lower panel of Figure 5, nonetheless, confirms rapid convergence in terms of spatial coverage, as the residual of Γ still follows the same $\sim r_{\text{cut}}^{-3}$ scaling law.

If the AGB outflow lasts for a $\sim 0.5 \times 10^5$ yr period, we can estimate the system will experience an extra $\sim 6\%$ orbital expansion using the measured average expansion rate. During this period, the expansion of the orbit should also take the mass-loss into account, which is estimated by the conservation of specific angular momentum,

$$\Lambda = [G(M_p + M_s)D]^{1/2} \sim \text{const} , \quad (9)$$

$$\frac{D_f}{D_i} \sim \frac{(M_p + M_s)_i}{(M_p + M_s)_f} ,$$

where the subscripts “i” and “f” stand for the initial and final values, respectively. Consider the fact that the mass-loss mainly takes place on the primary, after this time period, the percentage of orbit expansion due to reduced gravitation (from the $\sim 50\%$ AGB mass-loss) is $\sim 1/3$, and the “efficiency” of the trade between stellar mass and angular momentum is $\sim 20\%$.

4.2. Parameter Space and Applications

Similar to §4.2, we conduct four extra series of simulations to briefly survey how different hydrodynamic features impact the orbit evolution, each of which differs from the fiducial model by only one parameter. Results of these numerical experiments are presented in Table 2. We observe similar trends as §4.2 in terms of outflow dependencies, and find that the torque on the primary generally takes a negative share in the overall balance of Γ .

Table 2. Various models for AGB-pulsar binaries.

Series	Model	Description	Γ^* ($10^{-6} t_c^{-1}$)
0	A0	Fiducial	1.13 ± 0.86 [$-1.17 \pm 0.65, 2.31 \pm 1.01$]
1	A1-1	$\dot{M}_p = 3 \times$ Fiducial	2.54 ± 4.19 [$-3.25 \pm 1.90, 5.80 \pm 3.76$]
	A1-2	$\dot{M}_p = 0.3 \times$ Fiducial	-0.11 ± 0.19 [$-0.68 \pm 0.28, 0.57 \pm 0.16$]
2 [†]	A2-1	$v_{\text{src},s} = 0.1c$	0.63 ± 0.60 [$-1.68 \pm 0.68, 2.31 \pm 0.69$]
	A2-2	$v_{\text{src},s} = 0.033c$	1.46 ± 1.40 [$-0.96 \pm 0.59, 2.42 \pm 1.33$]
3 [‡]	A3	No AGB p_{rad}	-0.34 ± 0.07 [$-0.40 \pm 0.08, 0.06 \pm 0.02$]
4	A4	$M_s = 2 \times M_p$	0.58 ± 0.78 [$-1.10 \pm 0.59, 1.68 \pm 0.73$]

NOTE—*: The error shown after each data presents the standard deviation for time variation; the data in the second row for each model indicates the contribution to the overall (\dot{s}/s) from the primary (left) and the secondary (right).

†: Initial radial velocity of the pulsar wind is varied, while the primary wind speed is untouched.

‡: Implemented by including the full gravitational effects from the primary, in contrast to the recipes in the fiducial model that turns off the actual AGB gravitation to emulate an outflow driven by radiation pressure p_{rad} (§4.1).

As the lower-right panel in Figure 4 exhibits, the primary outflow materials dominate torques on both stars. Higher primary mass-loss rates generally enhance Γ by increasing torque exerted on the secondary, despite the offset torque on the primary also rising. Model A1-1, which follows the same logic, shows a sub-linear growth in the total torque, as the ratio of primary negative torque increase is greater than the secondary. Model A1-2, with 0.3 times the AGB outflow, yields a total negative torque that consists of a sharply reduced secondary torque and a primary negative torque that does not decline proportionally.

The same trend is also manifested in Series 2, illustrated by Figure 6. With higher pulsar wind speeds, the primary materials are pushed further from the pulsar but closer to the AGB, enhancing the primary negative torque and reducing the pulsar’s torque. Considering that the ram pressure is proportional to the total wind power at a fixed location, this sub-linear anti-correlation between Γ and the pulsar wind speed indicates that a relatively weaker pulsar wind \dot{E} is prone to the effect. Specifically, Model A3 reveals the importance of a sustained, radiation-driven AGB outflow in this scenario. Once the recipes for radiation pressure (i.e., zero effective gravity from the primary) is turned *off*, the AGB outflow will have a hard time reaching the vicinity of the pulsar and remove the base of the anti-friction ef-

fect. Model A4 has doubled primary mass: under the same mass loss rate, the period to lose $\sim 50\%$ of its mass is doubled to $\sim 10^5$ yr. Nevertheless, the eventual amplitude of orbit expansion is not significantly increased compared to the fiducial model, even if the integration time is doubled.

5. CONCLUSION AND DISCUSSIONS

This paper explores the role of the dynamical anti-friction effect in binary systems with isotropic outflows from both stars. We demonstrate that an equal mass binary system could gain angular momentum through dynamical anti-friction from the collision between outflows. The resulting expansion of the orbital radius has amplitude comparable to the expansion caused by the mass losses. For example, we have shown that the strong pulsar wind can cause the orbital expansion for an AGB-pulsar binary.

5.1. Factors on the Evolution of Orbit Size

By comparing numerical models, we find that outflows are crucial to cause the expansion of the orbit. In general, for each star in a binary, injecting a denser and slower outflow helps its companion to acquire a greater positive torque in two ways: first, shaping a denser “shell” between the bow shock and the terminal shock in front of a star for stronger forward gravity feedback; second, making the direction of net gravitation feedback force vector closer to tangential for a greater “useful” force component (see also §4.2). Nevertheless, the impact of denser outflows is not always monotonic. Because of the complicated fluid configurations modulated by orbital motion, quantitative analyses in, e.g., [Gruzinov et al. \(2020\)](#) is no longer accurate. Moreover, when the outflow is dense enough, it will push and “compress” the materials behind the gas shell and generate a denser “tail” that offsets the forward force to a greater extent. Meanwhile, the amount of material reserved for the outflows could be limited. Since the dynamical anti-friction effect often increases sub-linearly with \dot{M} , the total effects of ΔD could even decrease with increasing \dot{M} in the long run. Competition between these effects determines the eventual effects, requiring concrete calculations and discussions to specify.

Most cases in this paper that have positive Γ exhibit moderate ($\sim 10 - 30\%$) rates at which outflowing binaries “trade” their mass for orbital angular momenta. Because the mass loss will also result in the expansions of orbits due to weaker gravity, this is not an impressive efficiency. However, since the sign and amplitude of Γ depend on multiple outflow conditions, the evolution tracks for two subtly different binary systems

(although they could be pretty similar in many aspects at their initial stages) could be convergent or divergent. These effects have to be taken into account when one wants to infer the conditions of the progenitors from a fully-evolved binary. What is more, such evolution should also be found in the statistics of the evolved and evolving outflowing binary systems, suggesting more applications of this mechanism in a broader range of astrophysical systems. For example, measurements of the orbital properties for exoplanets are accurate down to $\lesssim 10^{-4}$ nowadays. In the following paper, we shall treat the systems of exoplanets and their host stars as a particular type of “binaries”, and further discuss the dynamic effects of the collision between the young-star stellar wind and the planet atmospheric outflows.

5.2. Scaling and Convergence of the Gravitational Effects

One of the common issues that one may raise upon the studies of dynamical (anti-)friction is the convergence of gravitational feedback. Because gravitation is a long-range interaction, correct asymptotes of gravity from materials at large distances are necessary to yield physically plausible conclusions; improper cut-offs would impair the reliability of results. The main concern in [Li et al. \(2020\)](#) is indeed the divergence of drag force coming from the gravitational wake due to the simplified assumption of infinite uniform ambient materials.

There is no such problem for simulations of colliding binary outflows presented in this paper. The scaling law of residual torque upon the cutoff radius r_{cut} drops below the r_{cut}^{-3} envelope, which is a good sign of convergence (see e.g. Figures 3 and 5). This scaling converges much faster than the $\sim r_{\text{cut}}^{-1}$ or even some divergent scalings in [Li et al. \(2020\)](#). We now prove that such r_{cut}^{-3} scaling is not a coincidence.

To prove the convergence, we focus on the far-field behavior of the gas. The wake of an outflow-outflow interaction region moves outwards following the shape of an arithmetic spiral (see Figure 7). In each $(0, 2\pi]$ period of the azimuthal angle φ along the spiral, the mass of this wake is simplified into the linear density distribution along the spiral line $R(\varphi; n) = R_{n+1} - \varphi\Delta R/(2\pi)$, where the subscript “ n ” marks the n th crossing of the $\varphi = 0$ radial line, and ΔR is the distance between adjacent loops. The mass perturbation per unit azimuthal angle satisfies $d(\delta m)/d\varphi \simeq \text{const}$, since the evolution of perturbation at large distances is mostly radial expansion.

Between the n -th and the $(n+1)$ -th crossing of the $\varphi = 0$ radial line, the net tangential force that the interested body feels can be estimated with simple trigonometries,

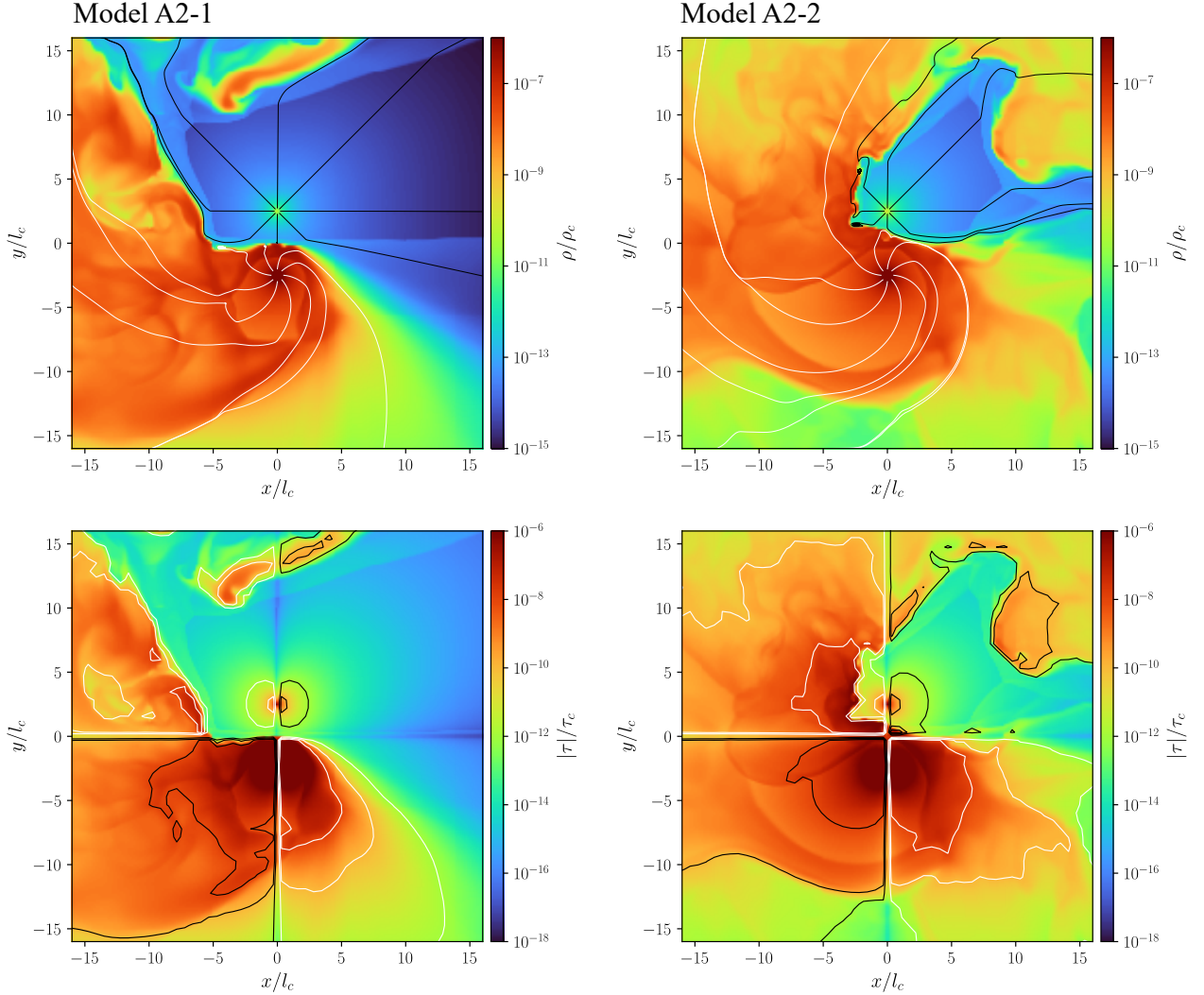


Figure 6. Zoomed-in plots for density (upper row) and torque density (lower row) of the $t \simeq 7 P$ snapshots for Models A2-1 ($v_{\text{src},s} = 0.1 c$, left column) and A2-2 ($v_{\text{src},s} = 0.033 c$, right column), respectively. Contours in the lower row are $\lg |\tau/\tau_c| \in \{-12, -10, -8\}$.

$$F_n \simeq -GM_* \left[\frac{d(\delta m)}{d\varphi} \right] \int_0^{2\pi} \frac{\sin \alpha d\varphi}{R'^2}, \quad (10)$$

where M_* is the object’s mass, b is the distance between the object and the center of mass. R' is the distance between the line segment and the object, and α is the direction angle of the line segment seen on the object’s perspective. These geometric quantities are given by the sine and cosine laws,

$$\begin{aligned} R'^2 &= R^2(\varphi; n) + b^2 - 2bR(\varphi; n) \cos \varphi, \\ \tan \alpha &= \tan \varphi - \frac{b}{R \cos \varphi}. \end{aligned} \quad (11)$$

Substituting eq. (11) into eq. (10), and expanding F_n to the leading-order of R , we find $F_n \sim O(R^{-3})$. Since $R \propto n$ at large n , the sum of the series $\{F_n\}$ converges rather quickly with this scaling. This convergence speed

is also applicable in realistic situations where the density perturbation is three-dimensional: the integral leading to this scaling is only modified by a bounded forming factor at the order of unity. From Figures 2 and 4, we can also confirm this point clearly from the τ (“torque density”) panels. All simulations involved in this work show that the spatial scaling for the residual gravitational effect upon the “cutoff” radius is indeed $O(r_{\text{cut}}^{-3})$. The outflow-collision scenario resolves the issue of divergence in the long-range nature of gravity.

5.3. Future Works

In addition to the AGB-pulsar binaries discussed in this paper, we envisage that dynamical anti-friction may also cause an orbital expansion in other systems, including the common envelope evolution and planet migration. This effect modifies our understanding of binary

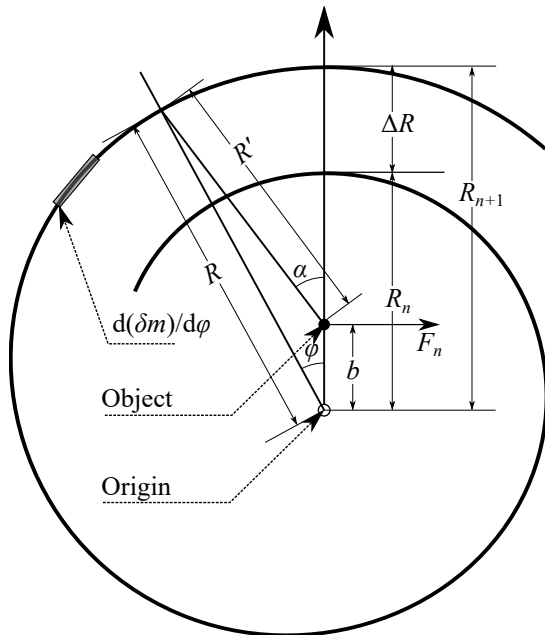


Figure 7. Schematic pattern of spiral-shaped far-field perturbation in colliding outflows and its impact to the concerned body. Geometric quantities concerned in §5 are all labelled in this figure.

evolution and may potentially impact the population modeling of binary compact object sources for gravitational waves. To simulate the common envelope evolution and planet systems need special numerical techniques, which are left for future works.

Our simulations employ a simple approach to assume isotropic winds are launched from the two stars without specifying the underlying mechanism. The outflow shuts off the accretion of materials onto the stars. In reality, the outflows from either stellar object may be accretion powered and may take the form of beamed jets that can reduce the effects of dynamical anti-friction (Li et al. 2020). Future studies are required to explore the dynamic effects of the combination of accretion and outflow.

Throughout our simulations, we assume the adiabatic gas equation of state. However, it is shown that gravitated outflows with adiabatic index $\gamma > 3/2$ cannot reach infinity (Parker 1958) and heating is generally a required factor to maintain a smaller effective γ , or equivalently a driving mechanism. Such heating could be rather complicated by radiative transfer, photochemistry, and thermochemistry. These details could modulate the thermodynamics dramatically, yielding considerable changes in the hydrodynamic circumstances that shape the collision between outflows. Specific to the AGB-pulsar binary models, both simulation and observation researchers suggest that AGB outflows are not steady, and significant pulsations could frequently occur (see e.g. Höfner & Olofsson 2018; Decin 2021, and references therein). More thorough and consistent studies in the future should treat the radiative transfer problem together with the dust grain formation problem within the AGB winds. We also notice that the interaction between magnetic fields can re-shape the stellar winds interactions system, including in the AGB-pulsar binaries. These details are temporarily ignored for more explicit analyses and presentations in this work and also reserve the colorfulness brought by these subtleties for future works.

L. Wang acknowledges the computation resources provided by the Kavil Institute of Astronomy and Astrophysics at Peking University. X. Li is supported by the Natural Sciences and Engineering Research Council of Canada (NSERC), funding reference #CITA 490888-16 and the Jeffrey L. Bishop Fellowship. Research at Perimeter Institute is supported in part by the Government of Canada through the Department of Innovation, Science and Economic Development Canada and the Province of Ontario through the Ministry of Colleges and Universities. The authors thank the helpful and inspiring discussions with our colleagues (alphabetical order of the last names), Zhuo Chen, Fei Dai.

REFERENCES

- Ackermann, M., Ajello, M., Baldini, L., et al. 2011, *ApJ*, 726, 35, doi: [10.1088/0004-637X/726/1/35](https://doi.org/10.1088/0004-637X/726/1/35)
- Antoni, A., MacLeod, M., & Ramirez-Ruiz, E. 2019, *ApJ*, 884, 22, doi: [10.3847/1538-4357/ab3466](https://doi.org/10.3847/1538-4357/ab3466)
- Bondi, H., & Hoyle, F. 1944, *MNRAS*, 104, 273, doi: [10.1093/mnras/104.5.273](https://doi.org/10.1093/mnras/104.5.273)
- Bosch-Ramon, V., Barkov, M. V., Khangulyan, D., & Perucho, M. 2012, *A&A*, 544, A59, doi: [10.1051/0004-6361/201219251](https://doi.org/10.1051/0004-6361/201219251)
- Chandrasekhar, S. 1943, *ApJ*, 97, 255, doi: [10.1086/144517](https://doi.org/10.1086/144517)
- Chen, Z., Blackman, E. G., Nordhaus, J., Frank, A., & Carroll-Nellenback, J. 2018, *MNRAS*, 473, 747, doi: [10.1093/mnras/stx2335](https://doi.org/10.1093/mnras/stx2335)
- Chen, Z., Frank, A., Blackman, E. G., Nordhaus, J., & Carroll-Nellenback, J. 2017, *MNRAS*, 468, 4465, doi: [10.1093/mnras/stx680](https://doi.org/10.1093/mnras/stx680)
- Chen, Z., Ivanova, N., & Carroll-Nellenback, J. 2020, *ApJ*, 892, 110, doi: [10.3847/1538-4357/ab7b6e](https://doi.org/10.3847/1538-4357/ab7b6e)
- De, S., MacLeod, M., Everson, R. W., et al. 2020, *ApJ*, 897, 130, doi: [10.3847/1538-4357/ab9ac6](https://doi.org/10.3847/1538-4357/ab9ac6)

- Decin, L. 2021, *ARA&A*, 59, 337,
doi: [10.1146/annurev-astro-090120-033712](https://doi.org/10.1146/annurev-astro-090120-033712)
- Edgar, R. 2004, *NewAR*, 48, 843,
doi: [10.1016/j.newar.2004.06.001](https://doi.org/10.1016/j.newar.2004.06.001)
- Eklund, H., & Masset, F. S. 2017, *MNRAS*, 469, 206,
doi: [10.1093/mnras/stx856](https://doi.org/10.1093/mnras/stx856)
- Fabrika, S. 2004, *Astrophys. Space Phys. Res.*, 12, 1,
<https://arxiv.org/abs/astro-ph/0603390>
- Gaensler, B. M. 2005, *Advances in Space Research*, 35, 1116, doi: [10.1016/j.asr.2005.01.026](https://doi.org/10.1016/j.asr.2005.01.026)
- Gruzinov, A., Levin, Y., & Matzner, C. D. 2020, *MNRAS*, 492, 2755, doi: [10.1093/mnras/staa013](https://doi.org/10.1093/mnras/staa013)
- Habing, H. J., & Olofsson, H. 2004, *Asymptotic Giant Branch Stars* (Springer, New York, NY),
doi: [10.1007/978-1-4757-3876-6](https://doi.org/10.1007/978-1-4757-3876-6)
- Hankla, A. M., Jiang, Y.-F., & Armitage, P. J. 2020, *ApJ*, 902, 50, doi: [10.3847/1538-4357/abb4df](https://doi.org/10.3847/1538-4357/abb4df)
- Höfner, S., & Olofsson, H. 2018, *A&A Rv*, 26, 1,
doi: [10.1007/s00159-017-0106-5](https://doi.org/10.1007/s00159-017-0106-5)
- Hoyle, F., & Lyttleton, R. A. 1939, *Proceedings of the Cambridge Philosophical Society*, 35, 405,
doi: [10.1017/S0305004100021150](https://doi.org/10.1017/S0305004100021150)
- Kley, W. 1998, *A&A*, 338, L37,
<https://arxiv.org/abs/astro-ph/9808351>
- Lamers, H. J. G. L. M., & Cassinelli, J. P. 1999, *Introduction to Stellar Winds* (Cambridge University Press)
- Li, X., Chang, P., Levin, Y., Matzner, C. D., & Armitage, P. J. 2020, *MNRAS*, 494, 2327,
doi: [10.1093/mnras/staa900](https://doi.org/10.1093/mnras/staa900)
- MacLeod, M., Antoni, A., Murguia-Berthier, A., Macias, P., & Ramirez-Ruiz, E. 2017, *ApJ*, 838, 56,
doi: [10.3847/1538-4357/aa6117](https://doi.org/10.3847/1538-4357/aa6117)
- Masset, F. S. 2017, *MNRAS*, 472, 4204,
doi: [10.1093/mnras/stx2271](https://doi.org/10.1093/mnras/stx2271)
- Masset, F. S., & Velasco Romero, D. A. 2017, *MNRAS*, 465, 3175, doi: [10.1093/mnras/stw3008](https://doi.org/10.1093/mnras/stw3008)
- Murray, D. W., Chang, P., Murray, N. W., & Pittman, J. 2017, *MNRAS*, 465, 1316, doi: [10.1093/mnras/stw2796](https://doi.org/10.1093/mnras/stw2796)
- Ostriker, E. C. 1999, *ApJ*, 513, 252, doi: [10.1086/306858](https://doi.org/10.1086/306858)
- Parker, E. N. 1958, *ApJ*, 128, 664, doi: [10.1086/146579](https://doi.org/10.1086/146579)
- Ramstedt, S., Schöier, F. L., Olofsson, H., & Lundgren, A. A. 2008, *A&A*, 487, 645,
doi: [10.1051/0004-6361:20078876](https://doi.org/10.1051/0004-6361:20078876)
- Schröder, S. L., MacLeod, M., Ramirez-Ruiz, E., et al. 2021, *arXiv e-prints*, arXiv:2107.09675,
<https://arxiv.org/abs/2107.09675>
- Shakura, N. I., Postnov, K. A., Kochetkova, A. Y., et al. 2015, *Astronomy Reports*, 59, 645,
doi: [10.1134/S1063772915070112](https://doi.org/10.1134/S1063772915070112)
- Stahler, S. W. 2010, *MNRAS*, 402, 1758,
doi: [10.1111/j.1365-2966.2009.15994.x](https://doi.org/10.1111/j.1365-2966.2009.15994.x)
- Toro, E. F. 2011, *Riemann Solvers and Numerical Methods for Fluid Dynamics: A Practical Introduction* (Springer, Berlin)
- Wilkin, F. P. 1996, *ApJL*, 459, L31, doi: [10.1086/309939](https://doi.org/10.1086/309939)